OGLE-2018-BLG-1700L: Microlensing Planet in Binary Stellar System

Cheongho Han[1] ⦿, Chung-Uk Lee[2,29], Andrzej Udalski[3,30], Andrew Gould[4,5,29], Ian A. Bond[6,31]
(LEADING AUTHORS),
Michael D. Albrow[7], Sun-Ju Chung[2,8] ⦿, Kyu-Ha Hwang[2] ⦿, Youn Kil Jung[2], Yoon-Hyun Ryu[2] ⦿, In-Gu Shin[2] ⦿,
Yossi Shvartzvald[9] ⦿, Jennifer C. Yee[10] ⦿, Weicheng Zang[11] ⦿, Sang-Mok Cha[2,12], Dong-Jin Kim[2], Hyoun-Woo Kim[2],
Seung-Lee Kim[2,8], Dong-Joo Lee[2], Yongseok Lee[2,12], Byeong-Gon Park[2,8], Richard W. Pogge[5] ⦿, M. James Jee[13,14], Doeon Kim[1]
(THE KMTNET COLLABORATION),
Przemek Mróz[3], Michał K. Szymański[3], Jan Skowron[3] ⦿, Radek Poleski[5], Igor Soszyński[3], Paweł Pietrukowicz[3] ⦿,
Szymon Kozłowski[3], Krzysztof Ulaczyk[15], Krzysztof A. Rybicki[3], Patryk Iwanek[3] ⦿, Marcin Wrona[3]
(THE OGLE COLLABORATION),
and
Fumio Abe[16], Richard Barry[17], David P. Bennett[17,18], Aparna Bhattacharya[17,18], Martin Donachie[19], Hirosane Fujii[16],
Akihiko Fukui[20,21] ⦿, Yoshitaka Itow[16] ⦿, Yuki Hirao[22], Yuhei Kamei[16], Iona Kondo[22] ⦿, Naoki Koshimoto[23,24] ⦿,
Man Cheung Alex Li[19], Yutaka Matsubara[16], Yasushi Muraki[16], Shota Miyazaki[22] ⦿, Masayuki Nagakane[22], Clément Ranc[17],
Nicholas J. Rattenbury[19] ⦿, Haruno Suematsu[22], Denis J. Sullivan[25], Takahiro Sumi[22], Daisuke Suzuki[26] ⦿, Paul J. Tristram[27],
Takeharu Yamakawa[16], and Atsunori Yonehara[28]
(THE MOA COLLABORATION)

[1] Department of Physics, Chungbuk National University, Cheongju 28644, Republic of Korea; cheongho@astroph.chungbuk.ac.kr
[2] Korea Astronomy and Space Science Institute, Daejon 34055, Republic of Korea
[3] Warsaw University Observatory, Al. Ujazdowskie 4, 00-478 Warszawa, Poland
[4] Max Planck Institute for Astronomy, Königstuhl 17, D-69117 Heidelberg, Germany
[5] Department of Astronomy, Ohio State University, 140 W. 18th Avenue, Columbus, OH 43210, USA
[6] Institute of Natural and Mathematical Sciences, Massey University, Auckland 0745, New Zealand
[7] University of Canterbury, Department of Physics and Astronomy, Private Bag 4800, Christchurch 8020, New Zealand
[8] Korea University of Science and Technology, 217 Gajeong-ro, Yuseong-gu, Daejeon, 34113, Republic of Korea
[9] IPAC, Mail Code 100-22, Caltech, 1200 E. California Boulevard, Pasadena, CA 91125, USA
[10] Center for Astrophysics | Harvard & Smithsonian 60 Garden Street, Cambridge, MA 02138, USA
[11] Physics Department and Tsinghua Centre for Astrophysics, Tsinghua University, Beijing 100084, People's Republic of China
[12] School of Space Research, Kyung Hee University, Yongin, Kyeonggi 17104, Republic of Korea
[13] Yonsei University, Department of Astronomy, Seoul, Republic of Korea
[14] Department of Physics, University of California, Davis, California, USA
[15] Department of Physics, University of Warwick, Gibbet Hill Road, Coventry, CV4 7AL, UK
[16] Institute for Space-Earth Environmental Research, Nagoya University, Nagoya 464-8601, Japan
[17] Code 667, NASA Goddard Space Flight Center, Greenbelt, MD 20771, USA
[18] Department of Astronomy, University of Maryland, College Park, MD 20742, USA
[19] Department of Physics, University of Auckland, Private Bag 92019, Auckland, New Zealand
[20] Instituto de Astrofísica de Canarias, Vía Láctea s/n, E-38205 La Laguna, Tenerife, Spain
[21] Department of Earth and Planetary Science, Graduate School of Science, The University of Tokyo, 7-3-1 Hongo, Bunkyo-ku, Tokyo 113-0033, Japan
[22] Department of Earth and Space Science, Graduate School of Science, Osaka University, Toyonaka, Osaka 560-0043, Japan
[23] Department of Astronomy, Graduate School of Science, The University of Tokyo, 7-3-1 Hongo, Bunkyo-ku, Tokyo 113-0033, Japan
[24] National Astronomical Observatory of Japan, 2-21-1 Osawa, Mitaka, Tokyo 181-8588, Japan
[25] School of Chemical and Physical Sciences, Victoria University, Wellington, New Zealand
[26] Institute of Space and Astronautical Science, Japan Aerospace Exploration Agency, 3-1-1 Yoshinodai, Chuo, Sagamihara, Kanagawa, 252-5210, Japan
[27] University of Canterbury Mt. John Observatory, P.O. Box 56, Lake Tekapo 8770, New Zealand
[28] Department of Physics, Faculty of Science, Kyoto Sangyo University, 603-8555 Kyoto, Japan
Received 2019 September 11; revised 2019 November 25; accepted 2019 November 29; published 2020 January 13

Abstract

We report a planet in a binary that was discovered from the analysis of the microlensing event OGLE-2018-BLG-1700. We identify the triple nature of the lens from the fact that the anomaly pattern can be decomposed into two parts produced by two binary-lens events, in which one binary pair has a mass ratio of ~ 0.01 between the lens components and the other pair has a mass ratio of ~ 0.3. We find two sets of degenerate solutions, in which one solution has a projected separation between the primary and its stellar companion less than the angular Einstein radius θ_E (close solution), while the other solution has a separation greater than θ_E (wide solution). From the Bayesian analysis with the constraints of the event timescale and angular Einstein radius, we find that the planet has a mass of $4.4^{+3.0}_{-2.0}\,M_J$ and the stellar binary components have masses of $0.42^{+0.29}_{-0.19}\,M_\odot$ and $0.12^{+0.08}_{-0.05}\,M_\odot$, respectively, and the distance to the lens is $D_L = 7.6^{+1.2}_{-0.9}$ kpc. The planet is a circumstellar planet according to the

---

wide solution, while it is a circumbinary planet according to the close solution.

Unified Astronomy Thesaurus concepts: Exoplanet systems (484); Binary stars (154)

1. Introduction

Since the first-generation microlensing experiments conducted in the early 1990s, e.g., the massive astrophysical compact halo object (MACHO; Alcock et al. 1993), Expérience pour la Recherche d'Objets Sombres (EROS; Aubourg et al. 1993), and Optical Gravitational Lensing Experiment I (OGLE-I; Udalski et al. 1994), the detection rate of microlensing events has dramatically increased. Compared to the rate of several dozens per year in the early stage, current lensing experiments, OGLE-IV (Udalski et al. 2015), Microlensing Observations in Astrophysics (MOA; Bond et al. 2001), and Korea Microlensing Telescope Network (KMTNet; Kim et al. 2016), annually report more than 3000 events. The greatly enhanced detection rate has become possible thanks to the increased monitoring cadence with the use of multiple telescopes equipped with large-format cameras.

With the increase of the event rate, the number of anomalous events, which exhibit deviations in lensing light curves from the standard form of a single-lens (1L) single-source (1S) event, has also increased. The most common case of anomalous events is binary-lens events, in which a single source is gravitationally lensed by a binary lens composed of two masses (2L1S). Binary-lens events are produced by various combinations of astronomical objects. As expected from the high stellar binary rate, the majority of 2L1S events are produced by binaries that are composed of two stars with similar masses. Binary-lens events are also produced by the star–planet combination, and this makes microlensing an important tool to detect extrasolar planets (Mao & Paczyński 1991; Gould & Loeb 1992), especially those located around and beyond the snow lines of faint M-dwarfs.

Although not very common, the number of events produced by triple lenses (3L1S events) is also increasing. By the time of writing this paper, there are nine published 3L1S events. Among them, five events were produced by multiplanet systems, including OGLE-2006-BLG-109 (Gaudi et al. 2008; Bennett et al. 2010), OGLE-2012-BLG-0026 (Han et al. 2013; Beaulieu et al. 2016), OGLE-2014-BLG-1722 (Suzuki et al. 2018), OGLE-2018-BLG-0532 (Ryu et al. 2019), and OGLE-2018-BLG-1011 (Han et al. 2019a).[32] We note that all of these microlensing multiplanetary systems were detected through the channel of central perturbations, in which the source passes close to the central magnification region around the host star of the planets (Griest & Safizadeh 1998). The high detection efficiency of this channel originates in the properties of lensing caustics induced by planetary companions. A planetary companion located around the Einstein ring of the host induces two sets of caustics, in which one set is located close to the host (central caustic) and the other set is positioned away from the host (planetary caustic). If a lens contains multiple planets, the individual planets induce central caustics in the common central region and affect the magnification pattern of the region. Then, the chance to detect multiple planets is high for high-magnification

events produced by the source approach close to the host of the planet (Gaudi et al. 1998).

Another population of the known triple-lens events are those produced by planets in binaries. These events include OGLE-2007-BLG-349 (Bennett et al. 2016), OGLE-2008-BLG-092 (Poleski et al. 2014), OGLE-2013-BLG-0341 (Gould et al. 2014), and OGLE-2016-BLG-0613 (Han et al. 2017). For OGLE-2008-BLG-092 and OGLE-2013-BLG-0341, the planets were identified by their own independent signals. Besides this independent channel, planets in binary systems can also be found through the central perturbation channel. This is possible because both planet and binary companions can induce caustics in a common region, which is the region around the planet-hosting binary star for a S-type planet (circumstellar planet) orbiting around one of the two widely separated binary stars and the region around the barycenter of the binary for a P-type planet (circumbinary planet) orbiting around the center of mass of the closely located binary stars. The microlensing planets OGLE-2007-BLG-349L(AB)c and OGLE-2016-BLG-0613L(AB)c were detected through this central perturbation channel.

Besides multiplanetary systems and planetary systems in binaries, triple lensing can also provide channels to probe various types of astronomical systems, such as triple stars and stars with a planet and a moon (Han & Han 2002; Han 2008; Liebig & Wambsganss 2010). From the analysis of the lensing event OGLE-2015-BLG-1459, Hwang et al. (2018) pointed out the possibility that the lens of the event was composed of a brown dwarf host, a Neptune-class planet, and a third body being a Mars-class object that could have been a moon of the planet.

Despite the usefulness in studying various astronomical objects, application of triple lensing is often hindered by the difficulty of analyzing events. This difficulty arises because triple-lens systems exhibit very complex caustic patterns such as nested and self-intersected caustics, and this results in lensing light curves of great diversity. Theoretically, the ranges of the critical curve topology and the caustic structure have not yet been fully explored, and thus the understanding about the lensing behavior of triple-lens systems is still incomplete (Rhie 2002; Daněk & Heyrovský 2015, 2019).

Fortunately, triple-lensing events can be readily analyzed for events produced by some specific cases of lens systems. These are the cases in which the 3L1S anomaly in the lensing light curve can be approximated by the superposition of the anomalies produced by two 2L1S events. Bozza (1999) and Han et al. (2001) pointed out that this superposition approximation could be used to analyze central perturbations induced by multiple planets. Lee et al. (2008) indicated that the approximation could also be applied for the detections and characterizations of planets in binary systems.

In this paper, we report the discovery of a new planet that belongs to a stellar binary system. The planetary system was found from the analysis of the microlensing event OGLE-2018-BLG-1700. The light curve of the event exhibits a complex pattern with multiple anomaly features. We identify the triple nature of the lens from the fact that the anomaly pattern can be decomposed into two parts produced by two 2L1S events.

The paper is organized as follows. In Section 2, we mention the acquisition and processing of data used in the analysis. In

---

[32] We note that the signals of two planets are securely detected for events OGLE-2006-BLG-109, OGLE-2012-BLG-0026, and OGLE-2018-BLG-1011. However, the signals of the second planets for the events OGLE-2014-BLG-1722 and OGLE-2018-BLG-0532 are rather less secure.

Section 3, we describe the analysis process that leads to the identification of the planet in a binary. We also present local solutions resulting from degeneracies. In Section 4, we characterize the source from its color and brightness. In Section 5, we estimate the physical lens parameters including the mass and distance to the lens. We summarize results and conclude in Section 6.

2. Observation and Data

The source star of the lensing event OGLE-2018-BLG-1700 is located toward the Galactic bulge field with the equatorial coordinates (RA, decl.) = (17:59:49.45, −28:31:43.1). The corresponding Galactic coordinates of the source are $(l, b) = (1°.93, −2°.47)$. The apparent baseline magnitude of the source is $I_{base} = 17.65$, but as we will show in Section 4, the source is heavily blended and it comprises only ∼9% of the baseline flux.

The lensing event was first found by the Optical Gravitational Microlensing Experiment (OGLE; Udalski et al. 2015) survey on 2018 September 15 (HJD′ ≡ HJD−2450000 ∼ 8376), which corresponded to the early stage of the source-flux brightening. The OGLE survey was conducted using the 1.3 m Warsaw Telescope located at the Las Campanas Observatory in Chile. OGLE observations of the event were done with a cadence of ∼2–3/nights using I- and V-band filters.

The event was also observed by the KMTNet (Kim et al. 2016) survey. The KMTNet survey was conducted utilizing three identical 1.6 m telescopes at the Siding Spring Observatory, Australia, Cerro Tololo Interamerican Observatory, Chile, and the South African Astronomical Observatory, South Africa. Hereafter, we refer to the individual KMTNet telescopes as KMTA, KMTC, and KMTS, respectively. The event was independently found from the analysis of the 2018 data conducted after the season (Kim et al. 2018) and it was designated as KMT-2018-BLG-2330. KMTNet observations of the event were carried out mostly in the I band with a 15 minute cadence for each telescope. Some V-band data were obtained mainly for the purpose of measuring the source color, but in our analysis, we include them in the analysis to maximize the coverage of the light curve. The KMTNet V-band data were obtained with a cadence corresponding to ∼1/10 of the I-band cadence.

There exist additional data from the MOA (Bond et al. 2001; Sumi et al. 2003) survey. The event was not alerted by the MOA survey but it was located in the middle of the their high-cadence fields. The MOA data were produced from the post-season photometry conducted for the source star found by other surveys. The MOA survey was done in a customized broad R band utilizing the 1.8 m telescope of the Mt. John Observatory in New Zealand.

Data used in the analysis are processed using the photometry codes developed based on the difference imaging technique (Alard & Lupton 1998) and customized by the individual survey groups: Woźniak (2000; OGLE), Albrow (2017; KMTNet), and Bond et al. (2001; MOA). We normalize the error bars of the individual data sets using the method of Yee et al. (2012). For a subset of KMTNet data (KMTC), we conduct additional photometry using the pyDIA photometry code (Albrow 2017) to measure the source color.

In Figure 1, we present the light curve of the event constructed with the combined data. The curve superposed on
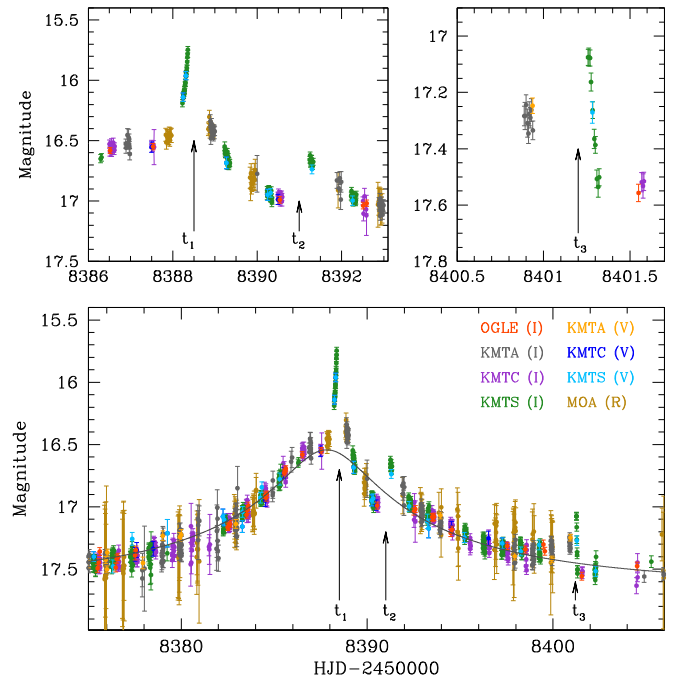

Figure 1. Light curve of the microlensing event OGLE-2018-BLG-1700. The lower panel shows the whole view of the event and the upper panels show zooms of the regions around the three peaks at the times marked by t_1, t_2, and t_3. The colors of the labels for the telescopes used for observations match those of the data points. The curve superposed on the data points is the model obtained from single-lens and single-source (1L1S) fitting of the data excluding the data points around the anomaly peak at t_1.

the data points in the lower panel shows the 1L1S model obtained by fitting the data excluding the data points around the anomaly peak at HJD′ ∼ 8388. The light curve shows a complex pattern of deviation from the 1L1S model. The deviation is characterized by three peaks that are centered at HJD′ ∼ 8388.2 (t_1), 8390.9 (t_2), and 8401.2 (t_3). We mark the individual peaks with arrows. In the upper two panels, we present the enlarged views of the peaks. The peaks at t_2 and t_3 together with the U-shape trough region between the peaks indicate that these peaks are produced by caustic crossings, in which the former and latter peaks occur when the source enters and exits the closed curve of a binary caustic, respectively. The peak at t_1, on the other hand, does not show a counterpart peak of the caustic-crossing pair. This suggests that the peak is likely to be produced by the source approach close to the cusp of a caustic.

3. Light Curve Modeling

3.1. 2L1S Analysis

Because the anomaly features in the light curve are likely to be involved with caustics, we start the modeling of the observed light curve with a model, in which a single source is lensed by a binary lens (2L1S). In 2L1S modeling, a basic description of the lensing light curve requires seven lensing parameters, including t_0, u_0, t_E, s, q, α, and ρ. The first three parameters (t_0, u_0, t_E) represent the time of the closest approach of the source to a reference position of the lens, the source-reference separation at that time, and the event timescale, respectively. We use the center of mass as a reference position

of the lens. The parameters (s, q) denote the projected binary separation and the companion/primary mass ratio, respectively, and α represents the angle between the source trajectory and the binary-lens axis. We note that the lengths of u_0 and s are normalized to the angular Einstein radius θ_E. The last parameter ρ indicates the ratio of the angular source radius θ_* to θ_E, i.e., $\rho = \theta_*/\theta_E$ (normalized source radius). The normalized source radius is needed to describe the caustic-crossing parts, during which the lensing magnifications are affected by finite-source effects.

Binary-lens modeling is conducted in two steps. In the first step, we conduct a grid search for the parameters s and q, while the other parameters are searched for using a downhill approach based on the Markov Chain Monte Carlo (MCMC) algorithm. Once a plausible local solution is found from this first-round search, we then refine the solution by allowing all lensing parameters to vary.

We find that 2L1S modeling does not yield a model explaining all the anomaly features despite repeated modeling runs with various combinations of the initial lensing parameters. In order to check the possibility that the anomaly could be described with higher-order effects, we consider two higher-order effects, including the microlens-lens parallax and the lens-orbital effects. The former effects occur due to the orbital motion of Earth (observer) around the Sun (Gould 1992) and the latter effects arise due to the orbital motion of the binary lens (Dominik 1998). Consideration of the microlens-parallax effect requires the inclusion of two additional lensing parameters of $\pi_{E,N}$ and $\pi_{E,E}$, which are the north and east components of the projected microlens-parallax vector, $\boldsymbol{\pi}_E$, in the equatorial coordinates, respectively. Consideration of the lens-orbital effects also requires the inclusion of two additional parameters of ds/dt and $d\alpha/dt$, which denote the instantaneous change rates (at t_1) of the binary separation and source trajectory angle, respectively. From these additional modeling runs, it is found that the anomaly features cannot be explained even with these higher-order effects.

3.2. 3L1S Analysis

Not being able to explain the light curve with 2L1S models, we then consider models, in which the lens is composed of three masses (3L). With the introduction of a third body M_3 in addition to the binary-lens components of M_1 and M_2, one needs to include additional lensing parameters. These parameters are the separation of the third body from the primary M_1, s_3, the mass ratio $q_3 = M_3/M_1$, and the orientation angle of M_3 as measured from the M_1–M_2 axis, ψ. We use the notations s_2 and q_2 to denote the M_1–M_2 separation and M_2/M_1 mass ratio, respectively.

Due to the large number of the 3L1S lensing parameters, which reaches 10, i.e., (t_0, u_0, t_E, s_2, q_2, α, s_3, q_3, ψ, ρ), not even considering higher-order effects, it is difficult to explore all of the parameter space. We, therefore, check the possibility of using the binary superposition approximation, in which the anomalies in the triple-lensing light curve are approximated by the superposition of the anomalies produced by the two hypothetical binary lensing events that would be produced by the M_1–M_2 and M_1–M_3 pairs. Under this approximation, we conduct 2L1S modeling for two sets of data, for each of which a part of the data is excluded. In the first data set, we exclude the data in the region $8387.0 < \text{HJD}' < 8389.5$, which corresponds to the region around the first anomaly centered at
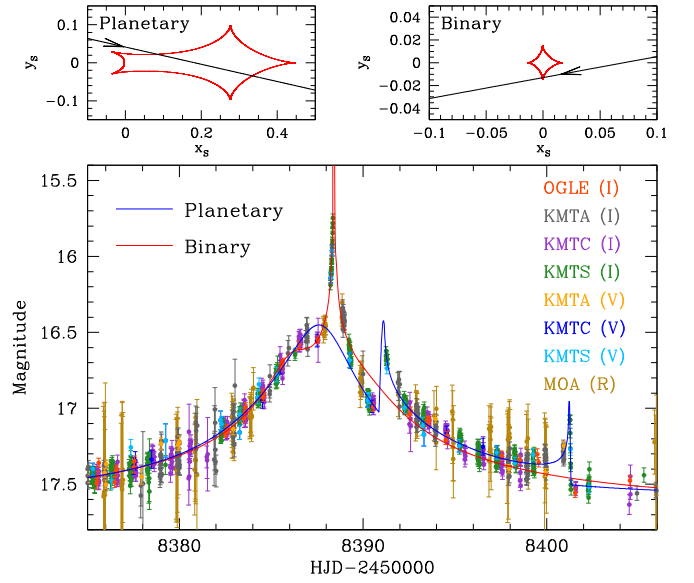

Figure 2. Decomposition of the anomaly into two parts produced by two binary-lens single-source (2L1S) events. The blue and red curves are the models of the 2L1S solutions obtained by fitting two sets of data, for each of which a part of the data is excluded. For the first data set, the data in the region $8387.0 < \text{HJD}' \equiv \text{HJD-2450,000} < 8395.5$ are excluded, while for the second set, the data in the region $8389.5 < \text{HJD}' < 8405.0$ are excluded. The 2L1S fit to the first data set results in a 2L1S solution (blue curve) with a very low mass ratio of $q \sim 0.01$, and thus we designate the model as planetary. The fit to the second data set (red curve), on the other hand, results in $q \sim 0.3$, and thus the solution is designated as binary. The upper panels show the lens system configurations of the planetary (left panel) and binary (right panel) solutions. For each panel, the closed concave curve represents the caustic and the line with an arrow indicates the source trajectory.

t_1. In the second data set, we exclude the data in the region $8389.5 < \text{HJD}' < 8405.0$, within which the pair of the caustic-crossing peaks at t_2 and t_3 are included.

In Figure 2, we present the two model light curves obtained from 2L1S fitting to the two separate data sets. The blue curve represents the model obtained from 2L1S fitting to the data set excluding the region around the peak at t_1, and the red curve is the model obtained from fitting to the data set excluding the caustic-crossing spikes at t_2 and t_3. We find that the anomalies are decomposed into two parts produced by the two 2L1S events, in which the blue model curve well describes the anomalies in the region including t_2 and t_3, while the red model curve explains the peak at t_1. This indicates that the event is produced by a lens with triple components and the anomaly in the lensing light curve can be well described by the binary superposition approximation. The binary parameters corresponding to the blue model curve are (s, q) $\sim$ (1.1, 0.01), indicating that the companion M_2 is a planetary mass object located near the Einstein radius of the primary-lens component M_1. For the model of the red curve, on the other hand, the mass ratio of the companion to the primary is $q \sim 0.3$, indicating that the third body M_3 is a stellar companion to the primary. We refer to the individual binary solutions as planetary and binary solutions, respectively. For the M_1–M_3 binary pair we find two solutions, in which one solution has a separation between the binary components much smaller than the Einstein radius ($s \ll 1.0$) and the other solution has a separation much greater than the Einstein radius ($s \gg 1.0$).

In the two upper panels of Figure 2, we present the lens system configurations of the planetary and binary 2L1S solutions. In each panel, the closed figure composed of
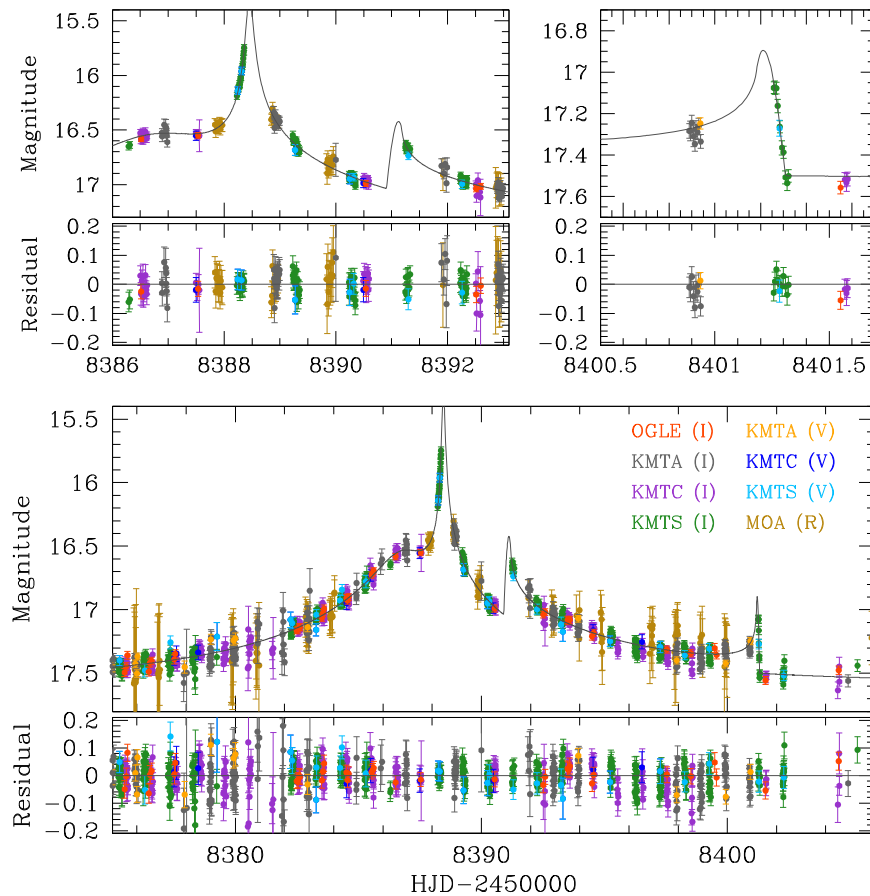
4

Figure 3. Model curve of the 3L1S solution. The upper panels show the enlarged views of the peak regions. The presented model is for the wide solution, in which the separation between M_1 and M_3 is greater than the Einstein radius, i.e., $s_3 > 1.0$. We note that the model curve of the close solution with $s_3 < 1.0$ is almost identical to the presented model curve of the wide solution.

concave curves represents the caustic and the line with an arrow represents the source trajectory. The caustics of the planetary solution form a single resonant hexalateral curve produced by a planetary companion. On the other hand, the caustics of the binary solution form a concave quadrilateral curve.

Using the lensing parameters of the two 2L1S solutions as initial parameters, we then conduct 3L1S modeling. In Figure 3, we present the best-fit 3L1S model curve superposed on the observed data points. It is found that the 3L1S solution well describes all the anomaly features. In Table 1, we present the lensing parameters of the 3L1S solution. We find that there exist two solutions resulting from the close/wide degeneracy in the M_1–M_3 separation, i.e., s_3, but we note that there is no close/wide degeneracy in the M_1–M_2 separation, i.e., s_2, because $s_2 \sim 1.0$ and thus the M_1–M_2 binary pair forms a resonant caustic. We note that the corresponding lensing parameters of the pair of degenerate solutions are similar to each other except that $s_{3,\mathrm{close}} \sim 1/s_{3,\mathrm{wide}}$. Hereafter, we designate the solutions with $s_3 > 1.0$ and $s_3 < 1.0$ as wide and close solutions, respectively. The degeneracy between the two solutions is relatively severe, with $\Delta\chi^2 = 2.7$.

In Figure 4, we present the lens system configurations of the 3L1S solutions, in which the upper and lower panels are for the wide and close solutions, respectively. For each of the solutions, the left panel shows the central magnification region, while the right panel shows the whole view including the locations of all the lens components. As expected from the

Table 1
Best-fit Lensing Parameters

Parameter	Wide ($s_3 > 1.0$)	Close ($s_3 < 1.0$)
t_0 (HJD′)	8386.152 ± 0.040	8385.827 ± 0.065
u_0 (10^{-3})	5.88 ± 0.66	6.70 ± 0.87
t_E (days)	43.12 ± 0.74	41.91 ± 0.82
s_2	1.019 ± 0.003	1.184 ± 0.003
q_2	0.010 ± 0.001	0.010 ± 0.001
α (rad)	3.432 ± 0.007	3.368 ± 0.007
s_3	3.823 ± 0.022	0.274 ± 0.003
q_3	0.274 ± 0.010	0.297 ± 0.009
ψ (rad)	5.525 ± 0.014	5.625 ± 0.015
ρ (10^{-3})	1.00 ± 0.07	0.95 ± 0.07

Note. HJD′ = HJD-2450,000.

severe degeneracy between the wide and close solutions, the lens system configurations in the central region of the two solutions are very similar to each other. From the investigation of the configurations, it is found that the overall pattern of the central caustic is similar to the resonant caustic produced by the M_1–M_2 pair of the 2L1S planetary solution, presented in the upper left panel of Figure 2. The source passes the caustic diagonally, crossing the upper left and lower right folds of the caustic, thereby producing the peaks at t_2 and t_3. The difference of the triple-lens caustic from that of the planetary 2L1S solution is that there exists a triangular-shape caustic in the central region near the location of the primary lens. We note
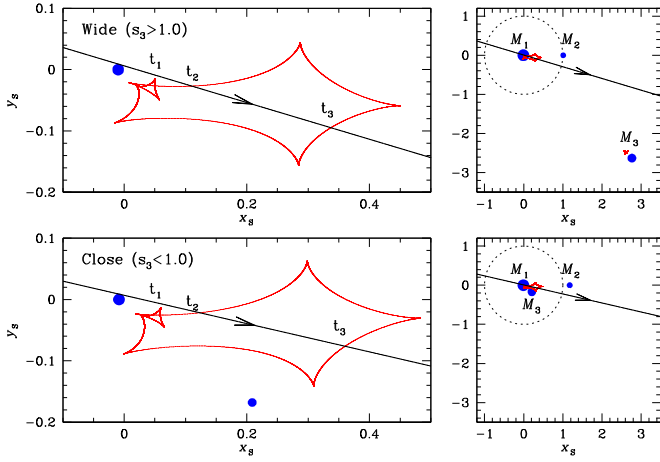
Figure 4. Lens system configurations of the 3L1S solutions. The upper and lower panels are for the wide ($s_3 > 1.0$) and close ($s_3 < 1.0$) solutions, respectively. For each solution, the left panel shows the central magnification region, while the right panel shows the whole view including the locations of all lens components, marked by M_1, M_2, and M_3. The positions on the source trajectory marked by t_1, t_2, and t_3 represent the source locations at the times of the three peaks in the lensing light curve marked in Figure 1. The dotted circle in each of the right panels represents the Einstein ring.

Figure 5. Comparison of models with and without the consideration of higher-order effects. The model curves of the two solutions are presented in the upper panel, in which the red and blue curves are for the solutions with and without higher-order effects, respectively. The lower panel shows the cumulative distributions of $\Delta\chi^2$ between the two solutions. The inset in the upper panel shows the zoomed-in region of $8392 \lesssim \mathrm{HJD}' \equiv \mathrm{HJD} - 2450{,}000 \lesssim 8400$, during which a major fit improvement occurs. The presented model light curves are for the solutions with $s_3 < 1.0$ and $u_0 > 0.0$.

that this caustic is nested and self-intersecting, and thus it appears to be different from the quadrilateral caustic of the binary 2L1S solution. The source approached close to one of the cusps of this central caustic, producing the peak that occurred at t_1. In the left panels of the figure, we mark three positions of the source, marked by t_1, t_2, and t_3, corresponding to the times of the three peaks in the light curve marked in Figure 1.

3.3. Higher-order Effects

We check the higher-order effects in the lensing light curve. Considering these effects is important not only for precisely describing the light curve but also for constraining the physical lens parameters because the mass and distance to the lens are related to the microlens parallax. In the modeling, we simultaneously consider both the microlens-parallax and lens-orbital effects because these effects can result in qualitatively similar deviations in lensing light curves (Batista et al. 2011; Skowron et al. 2011; Han et al. 2016). To consider the lens-orbital motion of the close solution, we use the approximation that the M_1–M_3 binary pair is orbiting around their center of mass and the planetary companion M_2 is orbiting around M_1. For the wide solution for which the binary companion, M_3, is located at a considerable distance from the primary, M_1, we consider only the orbital motion of the planetary companion around the primary-lens component, M_1.

In the lower panel of Figure 5, we present the cumulative distributions of the χ^2 difference between the two models obtained with and without considering the higher-order effects. The black curve is for the total data. The other curves are for the individual data sets, and the colors of the individual curves match those of the labels in the legend. We note that the data taken from each KMTNet telescope are composed of two sets because the source is located in the two overlapping fields (BLG03 and BLG43 fields) that are directed with a slight offset to fill the gaps between the chips of the camera. We also note that the MOA data set is not used for the higher-order modeling
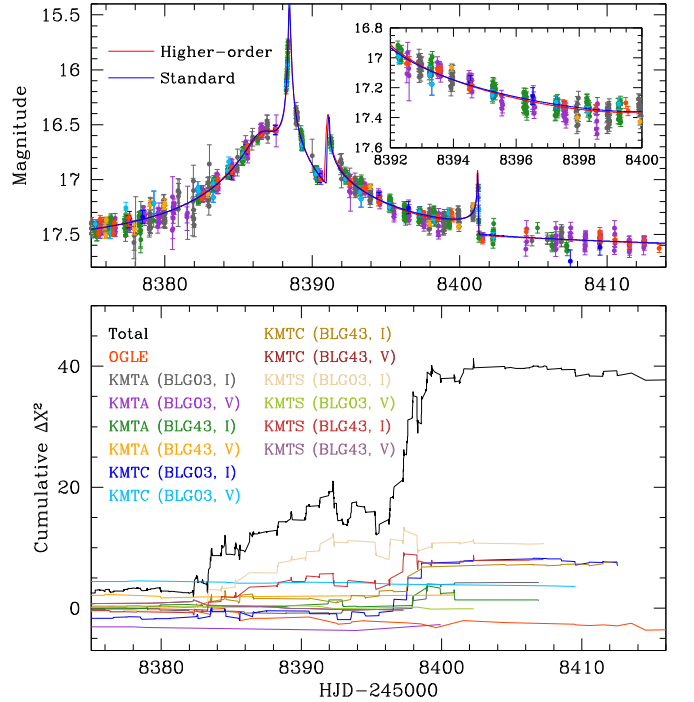
because of its relatively large photometric uncertainties. The presented model is for the close solution with $s_3 < 1.0$ and $u_0 > 0.0$. It is found that the consideration of the higher-order effects improves the fit by $\Delta\chi^2 \sim 38$. We note that the other degenerate solutions result in similar fit improvement. In the upper panel, we also present the model light curves obtained with (red curve) and without (blue curve) considering the higher-order effects. In the inset of the upper panel, we present a zoomed-in view of the region of $8392 \lesssim \mathrm{HJD}' \lesssim 8400$, during which a major fit improvement occurs.

We find that it is difficult to securely measure the higher-order effects. The main reason for the difficulty is caused by the subtlety of the deviation induced by the effects. This can be seen from the comparison of models with and without the effects presented in the upper panel of Figure 5, which shows that the two models result in very similar light curves. Due to the subtle deviation, the uncertainties of the measured higher-order lensing parameters are very large. In Figure 6, we present the $\Delta\chi^2$ distributions of MCMC points in the $\pi_{E,E}$–$\pi_{E,N}$ plane for the close (with $u_0 > 0.0$, left panel) and wide ($u_0 > 0.0$, right panel) solutions. The measured microlens-parallax parameters and their uncertainties are $(\pi_{E,N}, \pi_{E,E}) = (0.18 \pm 0.54, 0.23 \pm 0.14)$, $(\pi_{E,N}, \pi_{E,E}) = (-0.12 \pm 0.34, 0.11 \pm 0.12)$ for the close and wide solutions, respectively. As we will discuss in Section 5, these error bars are far larger than the constraints of the Bayesian analysis.

3.4. 2L2S Analysis

We additionally check solutions in which both the lens and source are binaries (2L2S). In this modeling, we hold the
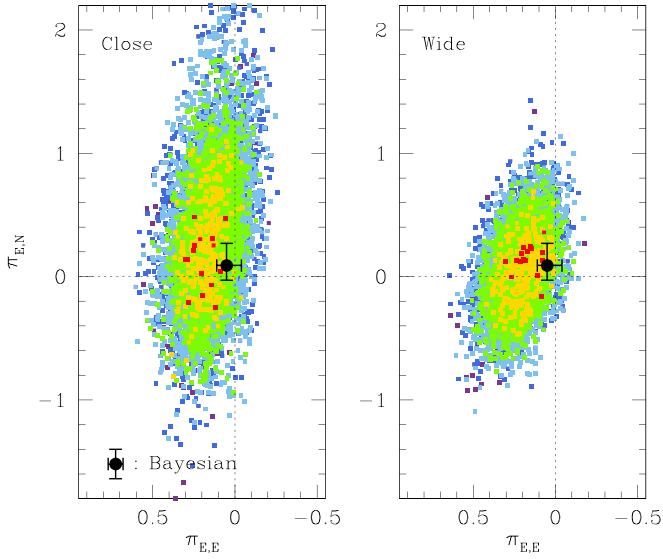
Figure 6. Distribution of $\Delta\chi^2$ of MCMC points in the $\pi_{E,E}-\pi_{E,N}$ plane for the close (with $u_0 > 0.0$, left panel) and wide ($u_0 > 0.0$, right panel) solutions. The color coding is set to represent points within 1σ (red), 2σ (yellow), 3σ (green), 4σ (cyan), 5σ (blue), and 6σ (purple). In each panel, the point with error bars represents the ranges of the microlens-parallax parameters estimated from the Bayesian analysis.

Figure 7. Positions of the source and blend with respect to the centroid of the red giant clump (RGC) in the instrumental color–magnitude diagram constructed based on the pyDIA photometry of the KMTNet BLG03 *I*- and *V*-band data.

trajectory of one source as that of the planetary 2L1S solution, which explains the peaks at t_2 and t_3, and test various trajectories of the other source to explain the peak at t_1. We find that the 2L2S modeling does not yield a solution that can explain the other peak at t_1, indicating that the 2L2S model cannot explain all the anomalous features in the observed lensing light curve.

4. Source Star

We characterize the source star by estimating its dereddened color, $(V-I)_0$, and brightness, I_0. The dereddened color and brightness are estimated from the instrumental values using the centroid of the red giant clump (RGC), for which its dereddened color, $(V-I)_{RGC,0}$, and brightness, $I_{RGC,0}$, are known, in the color–magnitude diagram (CMD) as a reference (Yoo et al. 2004).

In Figure 7, we mark the position of the source in the instrumental CMD constructed based on the pyDIA photometry of the KMTC *I*- and *V*-band data. We note that the instrumental *V* and *I* magnitudes are estimated using the regression of the data. The instrumental color and brightness of the source are $(V-I, I) = (2.31 \pm 0.03, 21.08 \pm 0.01)$ compared to the RGC centroid values of $(V-I, I)_{RGC} = (2.89, 16.29)$. From the offsets in color and brightness between the source and RGC centroid together with the known dereddened values $(V-I, I)_{RGC,0} = (1.06, 14.35)$ of the RGC centroid (Bensby et al. 2013; Nataf et al. 2013), the dereddened (calibrated) color and brightness of the source are estimated as

$$(V-I, I)_0 = (0.47 \pm 0.03, 18.96 \pm 0.01). \quad (1)$$

The color and brightness indicate that the source is an F-type main-sequence star. We note that the source color and brightness are subject to additional uncertainty caused by the uncertainty in determining the RGC centroid and the differential reddening of the field. Bensby et al. (2013) showed that for Galactic lensing events detected toward the bulge fields
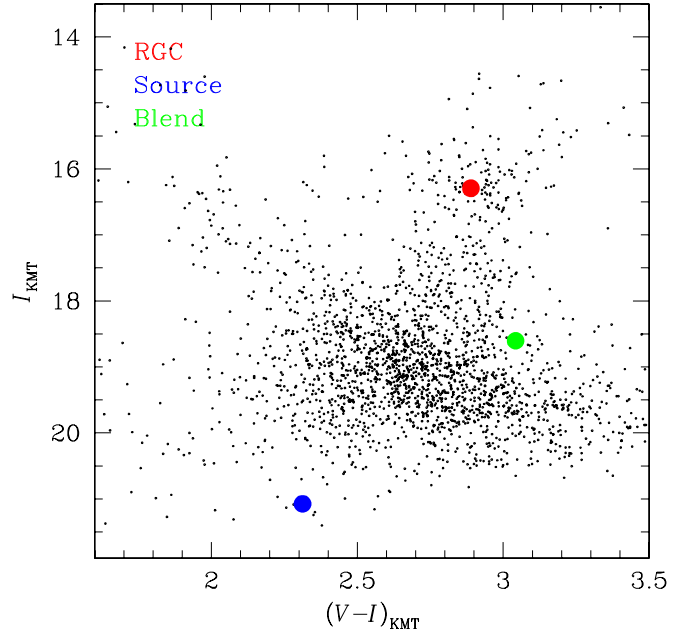
with well-defined RGCs, the typical error in the source color estimation is ~0.07 mag. We consider this additional error by adding a 7% error in quadrature when we estimate the angular source radius θ_*.

We determine the angular Einstein radius θ_E and the relative lens-source proper motion μ from the angular source radius θ_* that is estimated from the measured source color. For this, we first convert the measured $V-I$ color of the source into $V-K$ color using the color–color relation of Bessell & Brett (1988), and then estimate θ_* using the Kervella et al. (2004) relation between $V-K$ and θ_*. The estimated angular source radius is

$$\theta_* = 0.37 \pm 0.03 \ \mu\text{as}. \quad (2)$$

With the measured value of θ_*, the angular Einstein radius and the relative lens-source proper motions are estimated by

$$\theta_E = \frac{\theta_*}{\rho} = 0.37 \pm 0.04 \ \text{mas} \quad (3)$$

and

$$\mu = \frac{\theta_E}{t_E} = 3.13 \pm 0.30 \ \text{mas yr}^{-1}, \quad (4)$$

respectively.

We find that the source star is unlikely to be located in the bulge and, instead, it is most likely to be located in the far disk behind the bulge. According to the dereddened color, $(V-I)_0 \sim 0.47$, the source is an F-type star, but there are essentially no such bluish stars in the bulge. This indicates that the source is unlikely to be in the bulge and it should be located in the disk. A mid to late F-type star would be ~3–4 mag fainter than the clump giant if the source were located at the same distance as the clump giant. Considering that the source is ~4.8 mag fainter than the clump, it is likely that the source is located in the far disk behind the bulge. The Galactic latitude of the source is $b = -2°.47$. Hence, the line of sight passes about

415 pc below the disk plane at a source distance of
$D_S \sim 10$ kpc. Considering that the disk scale height is
$\sim$300 pc, there would be some disk stars at this height,
although the density is reduced.

Also marked in Figure 7 is the location of the blend. The
blend is $\sim$2.5 mag brighter than the source. We check the
possibility of the lens being the blend itself as in the case of
OGLE-2018-BLG-0740 (Han et al. 2019b). For this, we
measure the astrometric offset between the position of the
baseline object, measured in the image obtained by combining
72 KMTC images taken before lensing magnification, and the
position of the source, measured in the difference image
obtained by combining 47 difference images taken during
the lensing magnification. The measured offset is 0.60 pixels in
the chip of the KMTNet camera, which corresponds to 0″22. This
offset is much bigger than the astrometric errors in either the
position of the baseline object (0.04 pixels) or the difference
image (0.03 pixels). Therefore, the blend must be due at least in
part to an unrelated star or stars.

5. Lens System

For the unique determinations of the mass, M, and distance,
D_L, to the lens, it is required to measure both the microlens
parallax, π_E, and the angular Einstein radius, θ_E, which are
related to M and D_L by

$$M = \frac{\theta_E}{\kappa \pi_E}; \qquad D_L = \frac{\mathrm{au}}{\pi_E \theta_E + \pi_S}, \qquad (5)$$

where $\kappa = 4G/(c^2\mathrm{au})$ and $\pi_S = \mathrm{au}/D_S$ is the parallax to the
source, and D_S denotes the distance to the source. In the case
of OGLE-2018-BLG-1700, the angular Einstein radius is
measured, but the microlens parallax is not securely measured.
We, therefore, estimate the physical lens parameters by
conducting a Bayesian analysis of the event based on the
constraints of the measured event timescale and angular
Einstein radius together with the constraint of the source
location, i.e., far disk behind the bulge.

We conduct the Bayesian analysis using the prior models of
the lens mass function and the physical and dynamical
distributions of stars in the Galaxy. Based on these models,
we produce numerous artificial lensing events by conducting a
Monte Carlo simulation and construct the probability distribu-
tions of the lens mass and distance. In the analysis, we use the
Chabrier (2003) model for the mass function of stars and the
Gould (2000) model for the mass function of stellar remnants.
For the physical and dynamical distributions of matter, we use
the Han & Gould (2003) and Han & Gould (1995) models,
respectively. Among the produced events, the probability
distributions are constructed for events with timescales and
angular Einstein radii lying within the uncertainty ranges of the
measured t_E and θ_E, with disk source stars lying at distances of
$D_S \geqslant 8$ kpc. From the constructed probability distributions, we
then choose the physical parameters as the median values and
the uncertainties are estimated as the 68% ranges of the
distributions.

In the Monte Carlo simulation, we model the lens
distribution as that of the bulge. Because the source lies in
the far disk, the lens could in principle lie in either the far disk,
the bulge, or the near disk. However, the observed proper
motion of $\mu_{rel} = 3.1 \pm 0.3$ mas yr^{-1} virtually rules out near-
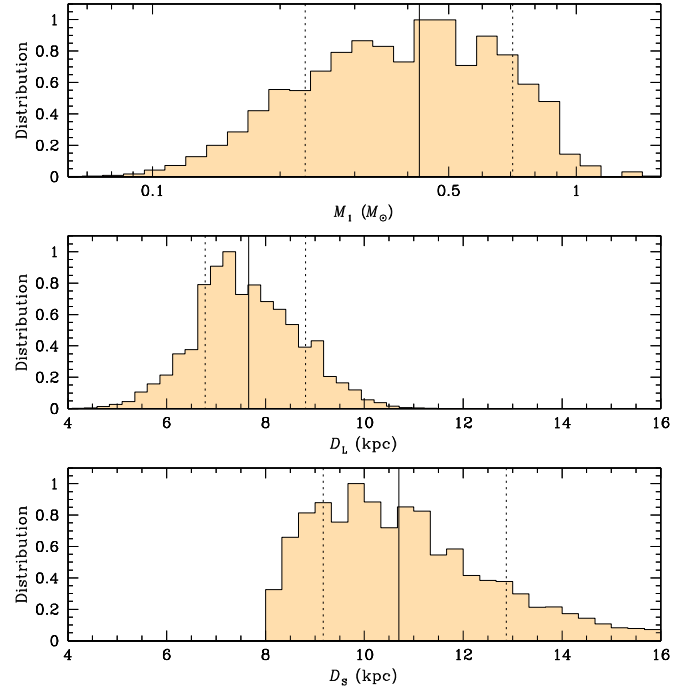

Figure 8. Probability distributions of the primary-lens mass, M_1 (top panel),
distance to the lens, D_L (middle panel), and the distance to the source, D_S
(bottom panel), obtained from the Bayesian analysis. For each distribution, the
solid vertical line represents the median value and the two dotted lines
represent the 68% range of the distribution. The distributions are for the wide
solution and the close solution results in nearly identical distributions.

disk lenses for which the expected mean proper motion would
be $\langle\mu_{rel}\rangle \simeq 2(v_{rot}/v_{rot}^2)/D_S \to 9.3$ mas yr^{-1} in the direction of
Galactic rotation. Only improbably large peculiar motions of
the lens or source (relative to the mean circular motion of the
Galactic disk) could then bring μ_{rel} within the observed range.
While far-disk lenses could in principle satisfy the proper-
motion constraint, the physical matter distribution along the
line of sight (and beyond the near disk) is completely
dominated by the bulge. We therefore model the lens
distribution as that of the bulge.

In Figure 8, we present the probability distributions of the
primary-lens mass, M_1, distance to the lens, D_L, and distance to
the source, D_S, obtained from the Bayesian analysis. In Table 2,
we summarize the physical lens parameters, including the
masses of the individual lens components (M_1, M_2, and M_3),
distances to the lens and source (D_L and D_S), and the projected
physical separations of M_2 and M_3 measured from the position
of M_1 ($a_{\perp,1-2}$ and $a_{\perp,1-2}$).

We find that the result from the Bayesian analysis is
consistent with the microlens-parallax measurement. For the
comparison of the parallax distributions, we compute the north
and east components of the microlens-parallax vectors π_E of
events produced by the Bayesian analysis as

$$\pi_{E,N} = \pi_{E,b}\cos\gamma + \pi_{E,l}\sin\gamma,$$
$$\pi_{E,E} = -\pi_{E,b}\sin\gamma + \pi_{E,l}\cos\gamma, \qquad (6)$$

respectively. Here $\gamma = 60°3$ represents the angle between arcs
of constant Galactic latitude (b) and constant equatorial decl.
(δ). The microlens-parallax components along the galactic
longitude (l) and latitude (b) directions are computed from the

Table 2
Best-fit Lensing Parameters

Parameter	Wide ($s_3 > 1.0$) Circumstellar	Close ($s_3 < 1.0$) Circumbinary
M_1 ($M_\odot$)	$0.42^{+0.29}_{-0.19}$	←
M_2 (M_J)	$4.40^{+3.04}_{-2.00}$	←
M_3 ($M_\odot$)	$0.12^{+0.08}_{-0.05}$	←
D_L (kpc)	$7.6^{+1.2}_{-0.9}$	←
D_S (kpc)	$10.7^{+2.2}_{-1.5}$	←
$a_{\perp,1-2}$ (au)	$2.8^{+3.2}_{-2.5}$	←
$a_{\perp,1-3}$ (au)	$10.5^{+12.1}_{-9.2}$	$0.75^{+0.87}_{-0.66}$

Note. M_1, M_2, and M_3 represent the masses of the individual triple-lens components, D_L and D_S denote the distances to the lens and source, respectively, and $a_{\perp,1-2}$ and $a_{\perp,1-3}$ represent the projected physical separations of between M_1–M_2 and M_1–M_3 pairs, respectively. The "←" symbols for the close solution imply that the values are the same as for the wide solution.

relative lens-source transverse velocity vector $\boldsymbol{v} = (v_l, v_b)$ by

$$\pi_{E,l} = \pi_E(v_l/v),$$
$$\pi_{E,b} = \pi_E(v_b/v). \qquad (7)$$

In Figure 6, we mark the ranges of $\pi_{E,N}$ and $\pi_{E,E}$ estimated from the Bayesian analysis as a dot with error bars superposed on the $\Delta\chi^2$ distribution of MCMC points obtained from light curve fitting. It is found that the Bayesian result is consistent with the microlens-parallax measurement, although the measurement uncertainty of π_E is large.

The interpretation of the planetary orbit varies depending on the solutions. According to the wide solution with $s_3 > 1.0$, the planet has an S-type orbit, in which the planet orbits around one of the two stellar binary stars, i.e., circumstellar planet. According to the close solution, on the other hand, the planet has a P-type orbit, in which the planet orbits around the barycenter of the close binary stars, i.e., circumbinary planet. We note that both the circumstellar and circumbinary planetary solutions result in similar ratios of the planet–host separation to the host–companion separation, i.e., ~0.27 for the circumstellar solution and ~0.23 for the circumbinary solution. Furthermore, the estimated separations are projected ones at the times of lensing magnifications. Therefore, it is difficult to conclude which solution is preferred based on the argument on the stability of planet orbit.

The planet is a super-Jupiter with a mass of

$$M_2 = 4.40^{+3.04}_{-2.00} \ M_J, \qquad (8)$$

and the stellar binary components are early and late M-type dwarfs with masses of

$$M_1 = 0.42^{+0.29}_{-0.19} \ M_\odot \qquad (9)$$

and

$$M_3 = 0.12^{+0.08}_{-0.05} \ M_\odot, \qquad (10)$$

respectively. The projected M_1–M_2 separation is

$$a_{\perp,1-2} = 2.8^{+3.2}_{-2.5} \ \text{au} \qquad (11)$$

for both the close and wide solutions. However, the projected M_1–M_3 separation estimated from the close solution,

$$a_{\perp,1-3} = 0.75^{+0.87}_{-0.66} \ \text{au} \qquad (\text{close}), \qquad (12)$$

is greatly different from the separation of

$$a_{\perp,1-3} = 10.5^{+12.1}_{-9.2} \ \text{au} \qquad (\text{wide}) \qquad (13)$$

estimated from the wide solution. The distance to the lens is

$$D_L = 7.6^{+1.2}_{-0.9} \ \text{kpc}, \qquad (14)$$

and the source is estimated to be in the far disk at a distance of

$$D_S = 10.7^{+2.2}_{-1.5} \ \text{kpc}. \qquad (15)$$

We note that it will be difficult to identify the lens by resolving the lens and source from high-resolution follow-up observations. This difficulty arises due to the combination of the slow relative lens-source proper motion, $\mu \sim 3.1$ mas yr^{-1}, and the faintness of the lens. Considering the mass, $M_1 \sim 0.42 \ M_\odot$, distance, $D_L \sim 7.6$ kpc, and extinction toward the field $A_I \sim 1.3$, the apparent brightness of the lens is $I \sim 23.8$, which is too faint to be detected as a flux excess.

6. Summary and Conclusion

We found a planet belonging to a stellar binary system from the analysis of the microlensing event OGLE-2018-BLG-1700. We identified the triple nature of the lens from the fact that the complex anomaly pattern could be decomposed into two parts produced by two binary-lens events, in which one binary pair had a very low mass ratio between the lens components and the other pair had similar masses. We found two sets of degenerate solutions, in which one solution had a projected separation between the stellar lens components less than the angular Einstein radius θ_E, while the other solution had a separation greater than θ_E. In order to estimate the physical lens parameters, we conducted a Bayesian analysis with the constraints of the measured event timescale and angular Einstein radius together with the location of the source lying in the far disk behind the bulge. From this, we found that the planet was a super-Jupiter with a mass of $4.4^{+3.0}_{-2.0} \ M_J$, and the stellar binary components were early and late M-type dwarfs with masses of $0.42^{+0.29}_{-0.19} \ M_\odot$ and $0.12^{+0.08}_{-0.05} \ M_\odot$, respectively. The interpretation of the planetary orbit varied depending on the solutions and the planet was a circumstellar planet orbiting around one of the two binary stars according to the wide solution, while it was a circumbinary planet orbiting around the center of mass of the binary stars according to the close solution.

ORCID iDs

Cheongho Han ⓘ https://orcid.org/0000-0002-2641-9964
Sun-Ju Chung ⓘ https://orcid.org/0000-0001-6285-4528
Kyu-Ha Hwang ⓘ https://orcid.org/0000-0002-9241-4117
Yoon-Hyun Ryu ⓘ https://orcid.org/0000-0001-9823-2907
In-Gu Shin ⓘ https://orcid.org/0000-0002-4355-9838
Yossi Shvartzvald ⓘ https://orcid.org/0000-0003-1525-5041
Jennifer C. Yee ⓘ https://orcid.org/0000-0001-9481-7123
Weicheng Zang ⓘ https://orcid.org/0000-0001-6000-3463
Richard W. Pogge ⓘ https://orcid.org/0000-0003-1435-3053
Jan Skowron ⓘ https://orcid.org/0000-0002-2335-1730
Paweł Pietrukowicz ⓘ https://orcid.org/0000-0002-2339-5899
Krzysztof Ulaczyk ⓘ https://orcid.org/0000-0001-6364-408X
Patryk Iwanek ⓘ https://orcid.org/0000-0002-6212-7221
Akihiko Fukui ⓘ https://orcid.org/0000-0002-4909-5763
Yoshitaka Itow ⓘ https://orcid.org/0000-0002-8198-1968
Iona Kondo ⓘ https://orcid.org/0000-0002-3401-1029
Naoki Koshimoto ⓘ https://orcid.org/0000-0003-2302-9562
Shota Miyazaki ⓘ https://orcid.org/0000-0001-9818-1513
Nicholas J. Rattenbury ⓘ https://orcid.org/0000-0001-5069-319X
Daisuke Suzuki ⓘ https://orcid.org/0000-0002-5843-9433

References

Alard, C., & Lupton, R. H. 1998, ApJ, 503, 325
Albrow, M. 2017, MichaelDAlbrow/pyDIA: Initial Release on Github, doi:10.5281/zenodo.268049
Alcock, C., Akerlof, C. W., Allsman, R. A., et al. 1993, Natur, 365, 621
Aubourg, E., Bareyre, P., Bréhin, S., et al. 1993, Natur, 365, 623
Batista, V., Gould, A., Dieters, S., et al. 2011, A&A, 529, 102
Beaulieu, J.-P., Bennett, D. P., Batista, V., et al. 2016, ApJ, 824, 83
Bennett, D. P., Rhie, S. H., Nikolaev, S., et al. 2010, ApJ, 713, 837
Bennett, D. P., Rhie, S. H., Udalski, A., et al. 2016, AJ, 152, 125
Bensby, T., Yee, J. C., Feltzing, S., et al. 2013, A&A, 549, 147
Bessell, M. S., & Brett, J. M. 1988, PASP, 100, 1134
Bond, I. A., Abe, F., Dodd, R. J., et al. 2001, MNRAS, 327, 868
Bozza, V. 1999, A&A, 348, 311
Chabrier, G. 2003, ApJL, 586, L133
Daněk, K., & Heyrovský, D. 2015, ApJ, 806, 99
Daněk, K., & Heyrovský, D. 2019, ApJ, 880, 72
Dominik, M. 1998, A&A, 329, 36
Gaudi, B. S., Bennett, D. P., Udalski, A., et al. 2008, Sci, 319, 927
Gaudi, B. S., Naber, R. M., & Sackett, P. D. 1998, ApJL, 502, L33
Gould, A. 1992, ApJ, 392, 442
Gould, A. 2000, ApJ, 535, 928
Gould, A., & Loeb, A. 1992, ApJ, 396, 10
Gould, A., Udalski, A., Shin, I.-G., et al. 2014, Sci, 345, 46
Griest, K., & Safizadeh, N. 1998, ApJ, 500, 37
Han, C. 2008, ApJ, 684, 684
Han, C., Bennett, D. P., Udalski, A., et al. 2019a, AJ, 158, 114
Han, C., Chang, H.-Y., An, J. H., & Chang, K. 2001, MNRAS, 328, 986
Han, C., & Gould, A. 1995, ApJ, 447, 53
Han, C., & Gould, A. 2003, ApJ, 592, 172
Han, C., & Han, W. 2002, ApJ, 580, 490
Han, C., Udalski, A., Choi, J.-Y., et al. 2013, ApJL, 762, L28
Han, C., Udalski, A., Gould, A., et al. 2017, AJ, 154, 223
Han, C., Udalski, A., Lee, C.-U., et al. 2016, ApJ, 827, 11
Han, C., Yee, J. C., Udalski, A., et al. 2019b, AJ, 158, 102
Hwang, K.-H., Udalski, A., Bond, I. A., et al. 2018, AJ, 155, 259
Kervella, P., Thévenin, F., Di Folco, E., & Ségransan, D. 2004, A&A, 426, 29
Kim, D.-J., Kim, H.-W., Hwang, K.-H., et al. 2018, AJ, 155, 76
Kim, S.-L., Lee, C.-U., Park, B.-G., et al. 2016, JKAS, 49, 37
Lee, D.-W., Lee, C.-U., Park, B.-G., et al. 2008, ApJ, 672, 623
Liebig, C., & Wambsganss, J. 2010, A&A, 520, 68
Mao, S., & Paczyński, B. 1991, ApJL, 374, L37
Nataf, D. M., Gould, A., Fouqué, P., et al. 2013, ApJ, 769, 88
Poleski, R., Skowron, J., Udalski, A., et al. 2014, ApJ, 795, 42
Rhie, S. H. 2002, arXiv:astro-ph/0202294
Ryu, Y.-H., et al. 2019, ApJ, submitted
Skowron, J., Udalski, A., Gould, A., et al. 2011, ApJ, 738, 87
Sumi, T., Abe, F., Bond, I. A., et al. 2003, ApJ, 591, 20
Suzuki, D., Bennett, D. P., Udalski, A., et al. 2018, AJ, 155, 263
Udalski, A., Szymański, J., Kałużny, J., et al. 1994, ApJL, 426, L69
Udalski, A., Szymański, M. K., & Szymański, G. 2015, AcA, 65, 1
Woźniak, P. R. 2000, AcA, 50, 421
Yee, J. C., Shvartzvald, Y., Gal-Yam, A., et al. 2012, ApJ, 755, 102
Yoo, J., DePoy, D. L., Gal-Yam, A., et al. 2004, ApJ, 603, 139